

A Full Bayesian Approach to SENSE Image Reconstruction Increases Brain Tissue Contrast and Reduces Noise for More Accurate Statistical Analysis

Chase J. Sakitis^a, D. Andrew Brown^b, Daniel B. Rowe^a

^a Department of Mathematical and Statistical Sciences, Marquette University, Milwaukee Wisconsin, USA

^b School of Mathematical and Statistical Sciences, Clemson University, Clemson, SC 29634, USA

Abstract

In fMRI, capturing cognitive temporal dynamics is dependent on how quickly volume brain images are acquired. The sampling time for an array of spatial frequencies to reconstruct an image is the limiting factor in the fMRI process. Multi-coil Sensitivity Encoding (SENSE) image reconstruction is a parallel imaging technique that has greatly reduced image scan time. In SENSE image reconstruction, coil sensitivities are estimated once from *a priori* calibration images and used as fixed “known” coil sensitivities for image reconstruction of every subsequent image. This technique utilizes complex-valued least squares estimation via the normal equation to estimate voxel values for the reconstructed image. This method can encounter difficulty in estimating voxel values when the SENSE design matrix is not positive definite. Here, we propose a Bayesian approach where prior distributions for the unaliased images, coil sensitivities, and uncertainty are assessed from the *a priori* calibration image information. Images and coil sensitivities are jointly estimated *a posteriori* via the Iterated Conditional Modes algorithm and Markov chain Monte Carlo using Gibbs sampling. In addition, variability estimates and hypothesis testing is possible. This Bayesian SENSE (BSENSE) model utilizes prior image information to reconstruct images from the posterior distribution and is applied to simulated and experimental fMRI data. This BSENSE model when compared to SENSE produced a cleaner, less noisy reconstructed image with a clearer distinction between the different brain matter. It also yielded increased task activation in both the simulated data and the experimental data.

Key Words: Bayesian, SENSE, fMRI, reconstruction

1. Introduction

1.1 Background

Magnetic Resonance Imaging (MRI) is a type of medical imaging that creates internal anatomic body images using strong magnetic fields. Functional Magnetic Resonance Imaging (fMRI) was developed in the early 1990’s as a technique to noninvasively observe the human brain in action without exogenous contrast agents (Bandettini et al, 1993). This procedure examines brain activity by detecting changes in the blood oxygenation using the blood-oxygen-level dependent (BOLD) contrast (Ogawa et al., 1990). When a neuron fires, the blood oxygenation changes in the proximity of the neuron and is thus a correlate for neuronal firing. In MRI, the machine does not directly measure voxel values and images. Measurements from the machine are arrays of complex-valued spatial frequencies called *k*-space (Kumar et al., 1975). Measuring full

arrays of data for all the slices that form the volume image typically takes about one to two seconds, limiting the temporal resolution of the acquired images. These k -space values are then reconstructed into images using an inverse Fourier transform (IFT). The acquisition of k -space arrays to make up a volume image can take a considerable amount of time. A great deal of work has been dedicated to reducing the scan time of the MRI process by accelerating the number of images acquired per unit of time. Hyde et al. (1986), Pruessmann et al. (1999), and Griswold et al. (2002) all explore parallel techniques to reduce the scan time in MRI.

1.2 Previous Approaches

Historically, a single channel coil receiver has been utilized in fMRI to measure full-sampled k -space data arrays. Along with parallel utilization of multiple receiver coils, parallel imaging techniques began subsampling lines in-plane by skipping lines of k -space for an image, causing the reconstructed coil images to be aliased. In 1999, Pruessmann et al. introduced SENSitivity Encoding (SENSE) which operates on the aliased images after the IFT. GeneRalized Autocalibrating Partial Parallel Acquisition (GRAPPA) is another parallel imaging technique, introduced by Griswold et al. (2002), that operates on the subsampled k -space prior to the IFT. Both are major parallel imaging techniques developed to unalias in-plane images. The purpose of this research is to introduce a formal Bayesian approach to SENSE (BSENSE) image reconstruction so the focus will be on SENSE.

As previously noted, acquiring a series of volume images can take a relatively long time and reducing scan time is a primary goal of parallel imaging. An intuitive solution to obtaining this goal is to travel faster through k -space. However, technical limitations of doing such have already been reached. This means the advancements in MRI technology has significantly reduced the intervals between the obtained spatial data, essentially maximizing the speed of the sequential data acquisition. More recently, the technology development focus has been to reduce time by measuring less data without losing the ability to form a full image. This can be accomplished by skipping lines in the k -space array and not measuring the corresponding data values which under-samples, or subsamples, k -space. Skipping lines in k -space introduces what is called an acceleration factor, or reduction factor. The acceleration factor indicates which lines of data in k -space are measured and how many lines are skipped in data acquisition. As shown in Figure 1.1

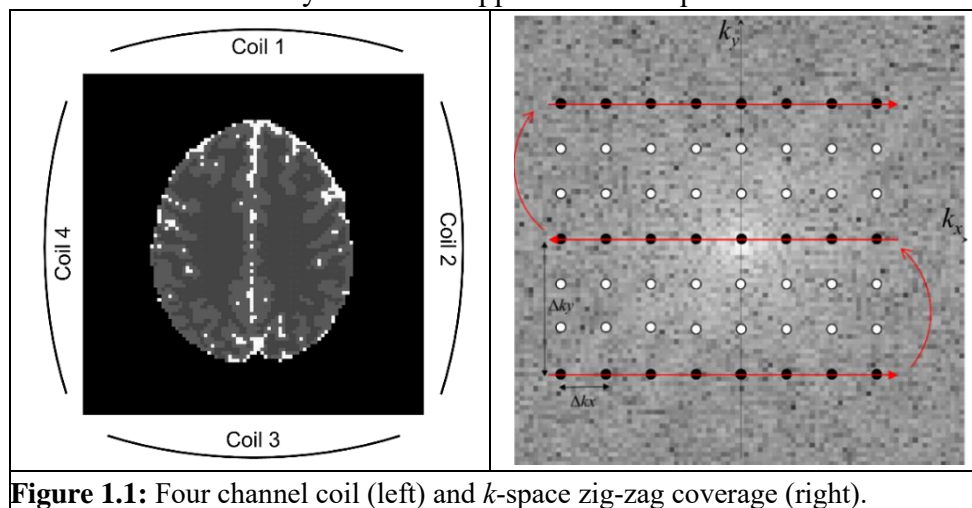


Figure 1.1: Four channel coil (left) and k -space zig-zag coverage (right).

(right), with an acceleration factor of $n_A = 3$, every third line horizontally in k -space is measured by skipping every two lines in the k -space array. This acceleration factor will cause the reconstructed coil images to appear as if the full image was cut into three equal horizontal strips that are summed together. This happens because the Fourier transform cannot uniquely map the insufficiently sampled signals. The SENSE method uses the sensitivity coil information to unfold and combine the aliased coil measurements into a full field-of-view (FOV) reconstructed image. This technique, however, can produce measurement noise in the reconstructed image which may require adding a regularizer to the parameter estimation or smoothing the images to reduce the noise. Also, SENSE only uses the sensitivity coil information from the calibration images for estimating the unaliased voxel values. With BSENSE, all valuable data from the calibration images, such as sensitivity coil weights, full FOV voxel values, noise variance, and the number calibration images, is employed as prior information. This prior information is utilized to estimate the unaliased voxel values while substantially reducing the contrast noise in the reconstructed image leading to more statistically significant task activation.

1.3 Overview

The second section of this paper will explain the model of SENSE image reconstruction and compare the complex-valued nature of the problem to a real-valued isomorphic representation. This will lead into our approach and the mathematics behind the Bayesian model in Section 3 along with hyperparameter assessment and parameter estimation. Section 4 will illustrate the simulated fMRI data for a single slice non-task image, discuss task activation, and show the results for task detection from a series of reconstructed images. This section will compare the simulated results between the SENSE method and the BSENSE method. In Section 5, we will describe the human fMRI data used for the experimental results of task detection. We will conclude in Section 6 with an overview of the important results of the paper, examine the advantages of BSENSE over SENSE, explore other aspects of BSENSE that were tested, and a discussion of future work.

2. SENSE Method

2.1 Model

Each local receiver coil possesses a depth sensitivity profile that is related to its size measuring a different sensitivity weighted version of the true slice. The use of $n_C = 4$ coils in this section and Section 3 are for illustration purposes only. The simulated and experimental results in Sections 4 and 5 will employ $n_C = 8$ receiver coils. Depicted in Figure 2.1 (middle center) is a true slice image with $n_A = 3$ voxels v_1, v_2, v_3 in corresponding locations relative to each strip. Each coil measures a rectangular k -space array that after inverse Fourier transform reconstruction produces an aliased rectangular image that is the weighted sum of three horizontal strips of the full true image. In Figure 2.1 (top right) the true aliased image is the point-wise multiplication of the given voxel by the sensitivity profile for coil 1 summed for the three strips, $a_1 = S_{11}v_1 + S_{12}v_2 + S_{13}v_3$ where S_{11} , S_{12} , and S_{13} are the scalar weights (valued between zero and one) that determines how strongly v_1 , v_2 , v_3 , respectively, show in coil 1 and a_1 is the scalar weighted voxel value (observed coil measurement). For each coil, the aliased sensitivities are not constrained to sum to one. For example, sensitivities S_{11} , S_{12} , and S_{13} from the top coil do not need to sum to one. Shown in Figure 2.1, this is the same process for the other three coils with coil 2 (bottom right) $a_2 = S_{21}v_1 + S_{22}v_2 +$

$S_{23}v_3$, coil 3 (bottom left) $a_3 = S_{31}v_1 + S_{32}v_2 + S_{33}v_3$, and coil 4 (top left) $a_4 = S_{41}v_1 + S_{42}v_2 + S_{43}v_3$. This is showing that a_1, a_2, a_3 , and a_4 are located in the same position (the white center point) in

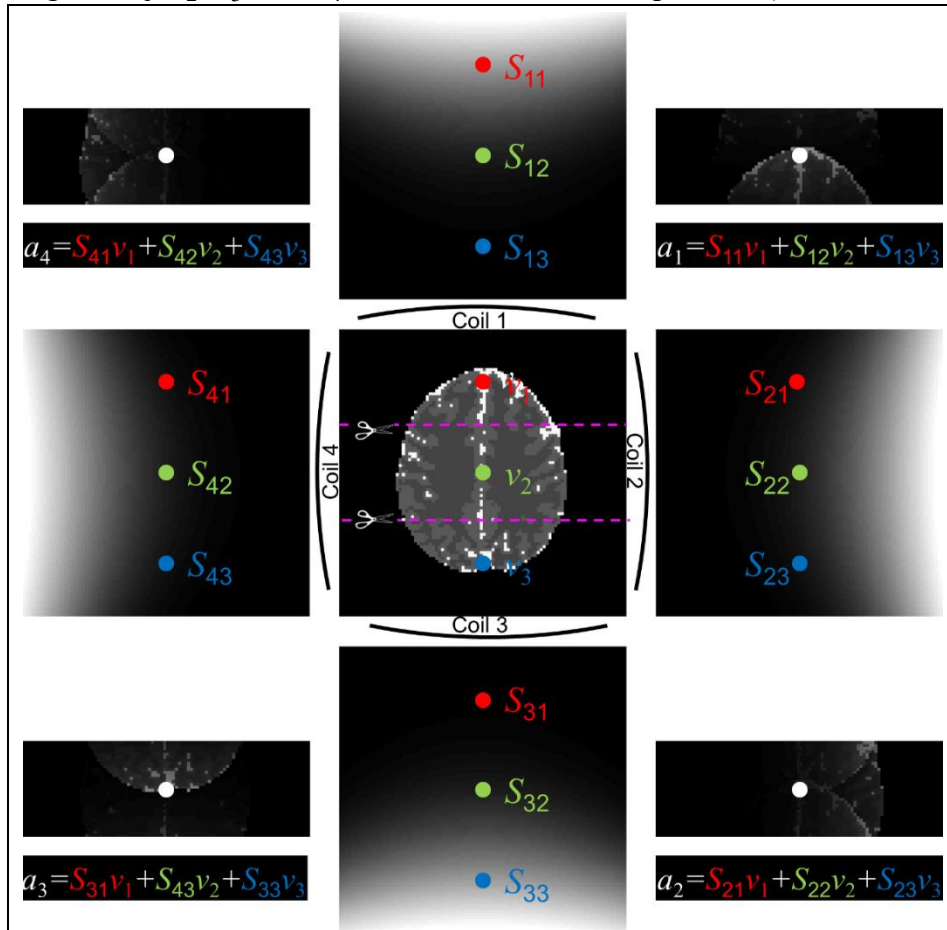


Figure 2.1: True slice image along with coil sensitivity profiles and sensitivity weighted true aliased images.

their respective aliased coil images which are used, along with coil measurements create a system of equations which can be expressed as Eq. 2.1.

$$\begin{bmatrix} a_1 \\ a_2 \\ a_3 \\ a_4 \end{bmatrix} = \begin{bmatrix} S_{11} & S_{12} & S_{13} \\ S_{21} & S_{22} & S_{23} \\ S_{31} & S_{32} & S_{33} \\ S_{41} & S_{42} & S_{43} \end{bmatrix} \begin{bmatrix} v_1 \\ v_2 \\ v_3 \end{bmatrix}. \quad [2.1]$$

Where $a = [a_1, a_2, a_3, a_4]'$ is a $n_C \times 1$ vector of the observed coil measurements, $S = [[S_{11}, S_{21}, S_{31}, S_{41}]', [S_{12}, S_{22}, S_{32}, S_{42}]', [S_{13}, S_{23}, S_{33}, S_{43}]']$ is a $n_C \times n_A$ matrix of the unobserved coil sensitivities, and $v = [v_1, v_2, v_3]'$ is a $n_A \times 1$ vector of the unobserved true slice voxel values. This system of equations can be represented by Eq. 2.2 and is the model used for SENSE image reconstruction.

$$a = Sv. \quad [2.2]$$

If we are able to obtain an estimate of the coil sensitivities \hat{S} from the pre-scan calibration images, we can obtain a least squares estimate of the n_A true slice voxel values v from Eq. 2.3.

$$\hat{v} = (\hat{S}'\hat{S})^{-1}\hat{S}'a. \quad [2.3]$$

This process is repeated for each voxel in the aliased image.

Since S is a matrix for the subsampling of k -space, the least squares estimation projects onto a subspace as opposed to the fully sampled k -space where S is a vector and the least squares estimation projects onto a vector so we must use caution when attempting to invert $(\hat{S}'\hat{S})$. This approach for parameter estimation can be difficult because the design matrix, generally, is ill-conditioned which means it is not always positive definite. This can cause signal-to-noise ratio (SNR) degradation and aliasing artifacts in the final reconstructed image when an acceleration (reduction) factor is applied (Pruessmann et al., 1999).

Rank deficiency or singularity in the design matrix can be a common problem in regression which can be mitigated using numerous techniques. In SENSE image reconstruction, the use of a regularizer is the most common approach to addressing issues with aliasing artifacts or SNR degradation. The regularization can still produce poor, low-resolution images that introduces bias resulting in blurred images [11]. Liu et al. (2009) used Bregman iterations to update the regularization function to reduce the effect from a fixed regularizer. In practice, however, this Bregman optimization can become computationally expensive increasing the reconstruction time. These deficiencies become the motivation for a Bayesian approach, which will allow for a more general method for image reconstruction, along with the use of available prior information, and provide full distributions for unknown parameters.

2.2 SENSE vs. SENSE-ITIVE

We now consider the true complex-valued version of the scenarios described in the previous subsection, as k -space data acquired by the MRI scanner is not real-valued. Traditional SENSE performs reconstruction while the data values are still in complex-valued form. Bruce et al. (2012) shows that the complex-valued model in Eq. 2.2 can be expressed by a real-valued isomorphic representation called the SENSE-ITIVE model conveyed by Eq. 2.4.

$$\begin{bmatrix} a_R \\ a_I \end{bmatrix} = \begin{bmatrix} S_R & -S_I \\ S_I & S_R \end{bmatrix} \begin{bmatrix} v_R \\ v_I \end{bmatrix}. \quad [2.4]$$

Eq. 2.4 characterizes the design matrix S as being skew-symmetric. The BSENSE model will use the real-valued isomorphism instead of the complex-valued representation (Bruce et al., 2012). Continuing the illustrative use of $n_C = 4$ receiver coils displayed in Figures 1.1 (left) and 2.1, the depth sensitivity profiles for each coil now contain a real part and an imaginary part. Each coil measures a complex-valued sensitivity weighted true image slice that is dependent on the location and size of the coil. Figure 2.2, similar to Figure 2.1 shows the true complex-valued image slices with $n_C = 4$ coils (top, bottom, left, right) and their respective depth sensitivity to the aliased true image slice (the four corners of the figure) with the real parts on the left and the imaginary parts on the right. In Figure 2.2 (top right) the aliased image is the point-wise multiplication of the given voxel by the sensitivity profile for coil 1 summed for the three strips. The linear equations for the real component and the imaginary component are expressed in Figure 2.2 (top right). This process is repeated for coil 2 (bottom right), coil 3 (bottom left), and coil 4 (top left), displayed in Figure 2.2, with the respective real and imaginary equations.

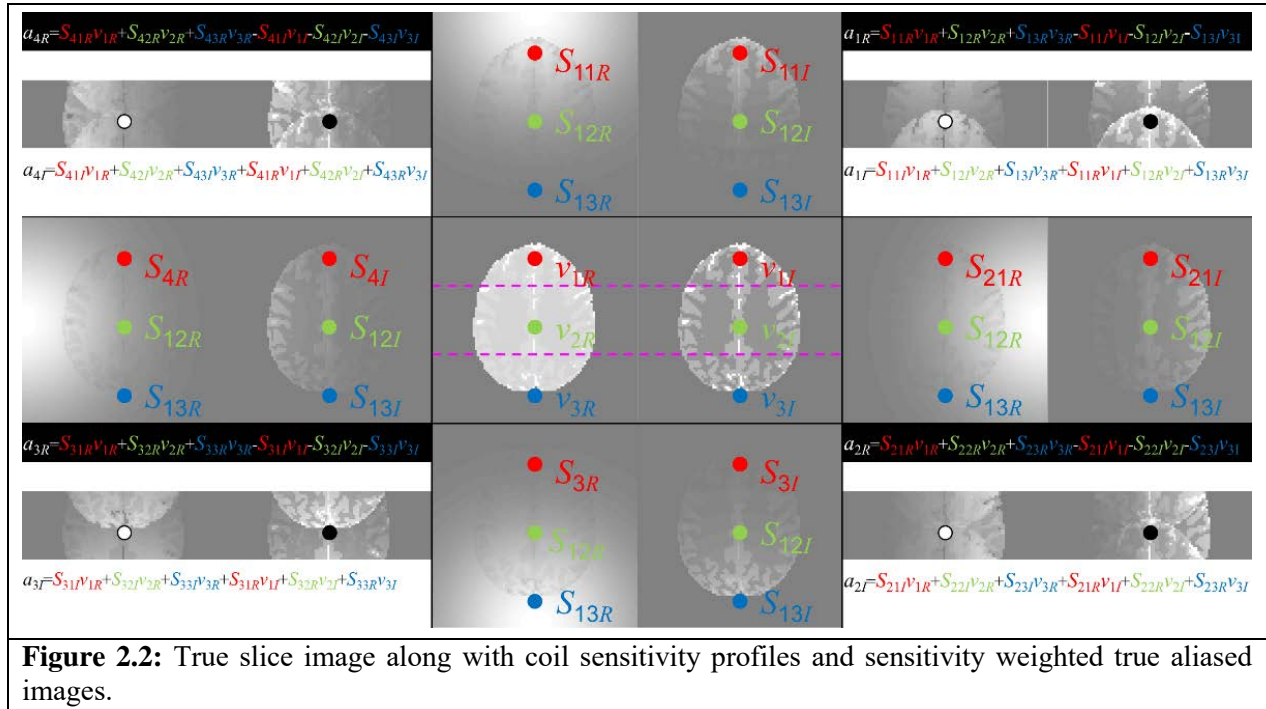


Figure 2.2: True slice image along with coil sensitivity profiles and sensitivity weighted true aliased images.

The $n_C = 4$ coil measurements create a system of equations which can be expressed in matrix form as shown in Eq. 2.5, where the a 's are observed aliased coil measurements, the S 's are unobserved coil sensitivities, and the v 's are unobserved true slice voxel values. Likewise in Eq. 2.4, this representation creates a skew symmetric design matrix for S . This equation is a latent variable model similar to factor analysis but complex-valued and can be more compactly written as $a = Sv$ where $a \in \mathbb{R}^{2n_C \times 1}$, $S \in \mathbb{R}^{2n_C \times 2n_A}$, and $v \in \mathbb{R}^{2n_A \times 1}$. We can obtain a least squares estimate of the n_A true slice voxel values v from Eq. 2.3 by estimating the complex-valued coil sensitivities \hat{S} and using the observed aliased coil measurements a .

$$\begin{bmatrix} a_{1R} \\ a_{2R} \\ a_{3R} \\ a_{4R} \\ a_{4I} \\ a_{2I} \\ a_{3I} \\ a_{4I} \end{bmatrix} = \begin{bmatrix} S_{11R} & S_{12R} & S_{13R} & -S_{11I} & -S_{12I} & -S_{13I} \\ S_{21R} & S_{22R} & S_{23R} & -S_{21I} & -S_{22I} & -S_{23I} \\ S_{31R} & S_{32R} & S_{33R} & -S_{31I} & -S_{32I} & -S_{33I} \\ S_{41R} & S_{42R} & S_{43R} & -S_{41I} & -S_{42I} & -S_{43I} \\ S_{11I} & S_{12I} & S_{13I} & S_{11R} & S_{12R} & S_{13R} \\ S_{21I} & S_{22I} & S_{23I} & S_{21R} & S_{22R} & S_{23R} \\ S_{31I} & S_{32I} & S_{33I} & S_{31R} & S_{32R} & S_{33R} \\ S_{41I} & S_{42I} & S_{43I} & S_{41R} & S_{42R} & S_{43R} \end{bmatrix} \begin{bmatrix} v_{1R} \\ v_{2R} \\ v_{3R} \\ v_{1I} \\ v_{2I} \\ v_{3I} \end{bmatrix}. \quad [2.5]$$

It is important to note that $(\hat{S}'\hat{S})$ in Eq. 2.3 is not generally positive definite and can be nearly singular due to it being ill-conditioned making it numerically unstable to invert. The design and construction of the sensitivity coils can cause the columns of S to be nearly linearly dependent. This problem can sometimes be mitigated using a regularizer such as lasso (Tibshirani, 1996) or ridge regression (Hoerl, Kennard, 1970). Liu et al. (2009) also used Bregmans distance to update the regularizer but the iteration algorithm can be computationally expensive. These regularizers are derived from Bayesian statistics, so an overarching Bayesian approach is appropriate for addressing the problem. Using a Bayesian approach offers more insight into hyperparameter

assessment and increased flexibility in parameter estimation by treating the design matrix as an unknown parameter to be assessed along with the unaliased voxel values and the noise. We can obtain the Maximum *A Posteriori* (MAP) estimate using the Iterated Conditional Modes (ICM) algorithm. The MAP estimate offers us a single data point, similar to that of the least squares estimation using a regularizer, however the Bayesian framework utilizes more prior information from the calibration images. A Markov chain Monte Carlo (MCMC) estimation technique such as Gibbs sampling can be used to assess the full posterior distribution of the unknown design matrix (coil sensitivities S), unaliased voxel values v , and the noise variance. This means that any statistical analysis can be performed to estimate the parameters, such as marginal posterior means. With a Bayesian approach, any and all prior information about our unknown parameters obtained from the calibration images can be used to assess the hyperparameters and estimate the parameters, unaliasing the folded images.

3. Bayesian Approach to SENSE (BSENSE)

For the Bayesian approach, the observed aliased voxels will use the same model that SENSE-ITIVE uses. That is $a = Sv + \varepsilon$ where $a \in \mathbb{R}^{2n_C \times 1}$, $S \in \mathbb{R}^{2n_C \times 2n_A}$, $v \in \mathbb{R}^{2n_A \times 1}$, and $\varepsilon \in \mathbb{R}^{2n_C \times 1}$. Two different representations of the coil sensitivities will be used. The first representation is $S \in \mathbb{R}^{2n_C \times 2n_A}$ as demonstrated in Eq. 2.5 is necessary for the proper skew symmetric design matrix for complex-valued multiplication. The second is $H \in \mathbb{R}^{2n_C \times n_A}$, as shown in Eq. 3.1, is used as the representation for the prior distribution and ultimately for parameter estimation of the coil sensitivities.

$$H = \begin{bmatrix} S_{11R} & S_{21R} & S_{31R} & S_{41R} \\ S_{12R} & S_{22R} & S_{32R} & S_{42R} \\ S_{13R} & S_{23R} & S_{33R} & S_{43R} \\ S_{11I} & S_{21I} & S_{31I} & S_{41I} \\ S_{12I} & S_{22I} & S_{32I} & S_{42I} \\ S_{13I} & S_{23I} & S_{33I} & S_{43I} \end{bmatrix}. \quad [3.1]$$

Using the H representation of the sensitivities will ensure that the real and imaginary components only get estimated once since they only appear once in the H depiction. This preserves the proper skew symmetry constraint of the *a posteriori* estimated sensitivities.

3.1 Data Likelihood, Prior and Posterior Distributions

Similar to SENSE, it is assumed that the residual error in real and imaginary are normally distributed. The likelihood distribution for the measurements become

$$P(a | S, v, \sigma^2) \propto (\sigma^2)^{-\frac{2n_C}{2}} \exp \left[-\frac{1}{2\sigma^2} (a - Sv)'(a - Sv) \right] \quad [3.2]$$

where a is the observed aliased coil image measurements, S is the unobserved coil reception sensitivities, v is the unobserved true image slice voxel values, and σ^2 is the unobserved image noise variance.

We can quantify available prior information about the unobserved parameters S , v , and σ^2 in the likelihood with assessed hyperparameters of prior distributions. The coil sensitivities

represented as H and the voxel values v are specified to have normal prior distributions and the noise variance σ^2 is specified to have an inverse gamma prior distribution i.e.,

$$P(H | n_S, H_0, \sigma^2) \propto (\sigma^2)^{-\frac{2n_c n_A}{2}} \exp\left[-\frac{n_S}{2\sigma^2} \text{tr}[(H - H_0)'(H - H_0)]\right] \quad [3.3]$$

$$P(v | n_v, v_0, \sigma^2) \propto (\sigma^2)^{-\frac{2n_A}{2}} \exp\left[-\frac{n_v}{2\sigma^2} (v - v_0)'(v - v_0)\right] \quad [3.4]$$

$$P(\sigma^2 | \alpha, \beta) \propto (\sigma^2)^{-(\alpha+1)} \exp\left[-\frac{\beta}{\sigma^2}\right] \quad [3.5]$$

with hyperparameters $n_S, H_0, n_v, v_0, \alpha,$ and β to be assessed from the pre-scanned calibrated images. By combining the likelihood distribution and the prior distributions, the posterior distribution of the coil sensitivities S , the true slice voxel values v , and the noise variance σ^2 is

$$P(H, v, \sigma^2 | a) \propto P(a | S, v, \sigma^2)P(H | n_S, H_0, \sigma^2)P(v | n_v, v_0, \sigma^2)P(\sigma^2 | \alpha, \beta) \quad [3.6]$$

with the distributions specified from Equations 3.2, 3.3, 3.4, and 3.5.

3.2 Parameter Estimation

Using the posterior distribution in Eq. 3.6 with the priors described in Equations 3.3, 3.4, and 3.5 along with the likelihood distribution in Eq. 3.2, two techniques are used to estimate the unobserved parameters $S, v,$ and σ^2 : Maximum A Posteriori (MAP) estimation using the Iterated Conditional Modes (ICM) optimization algorithm (Lindley and Smith, 1972) to find the posterior mode, and marginal posterior estimates via a Markov chain Monte Carlo (MCMC) Gibbs sampler (Geman and Geman, 1984; Gelfand and Smith 1990). Beginning with initial estimates of each parameter, ICM iterates over the parameters calculating its posterior conditional mode and converges to a global maximum of the joint posterior density. Since each of the posterior conditionals are unimodal, the ICM will produce the global maximum, the MAP, instead of the local maximum. The posterior conditional modes for the parameters are

$$\hat{v} = (S'S + n_v I_{2n_A})^{-1} (S'a + n_v v_0) \quad [3.7]$$

$$\hat{H} = (C'C + n_S I_{2n_A})^{-1} (CY' + n_S H_0) \quad [3.8]$$

$$\hat{\sigma}^2 = \frac{(a - Sv)'(a - Sv) + n_v (v - v_0)'(v - v_0) + \alpha\beta + n_S \text{tr}[(S - S_0)(S - S_0)]}{2(2n_c + 2n_A + \alpha + 2n_c n_A + 1)}. \quad [3.9]$$

It can be shown that the full conditional distributions of each parameter $S, v,$ and σ^2 for the MCMC Gibbs sampler are given by

$$v | S, \sigma^2, a \sim N(\hat{v} = (S'S + n_v I_{2n_A})^{-1} (S'a + n_v v_0), \sigma^2 (S'S + n_v I_{2n_A})^{-1}) \quad [3.10]$$

$$H | v, \sigma^2, a \sim MN(\hat{H} = (C'C + n_S I_{2n_A})^{-1} (CY' + n_S H_0), I_{n_c}, \sigma^2 (C'C + n_S I_{2n_A})^{-1}) \quad [3.11]$$

$$\sigma^2 | v, S, a \sim IG(\alpha_*, \beta_*) \quad [3.12]$$

where $\alpha_* = n_c n_A + n_c + n_A + \alpha,$ $\beta_* = 0.5[(a - Sv)'(a - Sv) + n_v (v - v_0)'(v - v_0) + n_S \text{tr}((H - H_0)'(H - H_0)) + 2\beta],$ and $Y \in \mathbb{R}^{2n_c \times 2}$ observed coil measurements having the real part in the first column and

the imaginary part in the second column as such $[a_R, a_I]$. In addition, a skew-symmetric $C \in \mathbb{R}^{2 \times 2n_A}$ is utilized with unaliased voxel values as expressed in Eq. 3.13,

$$C = \begin{bmatrix} v_{1R} & v_{2R} & v_{3R} & -v_{1I} & -v_{2I} & -v_{3I} \\ v_{1I} & v_{2I} & v_{3I} & v_{1R} & v_{2R} & v_{3R} \end{bmatrix}. \quad [3.13]$$

3.3 Hyperparameter Determination

Prior to an fMRI experiment, a short non-task based set of $n_{cal} = 10$ full k -space volume images for the n_C coils can easily be obtained. These calibration images can be utilized to assess appropriate hyperparameters for the prior distribution. For this experiment, the calibration images were simulated by adding $N(0,0.01)$ noise to the real and imaginary parts of the true complex-valued image slice that was multiplied by a designed sensitivity map. This is to accurately resemble

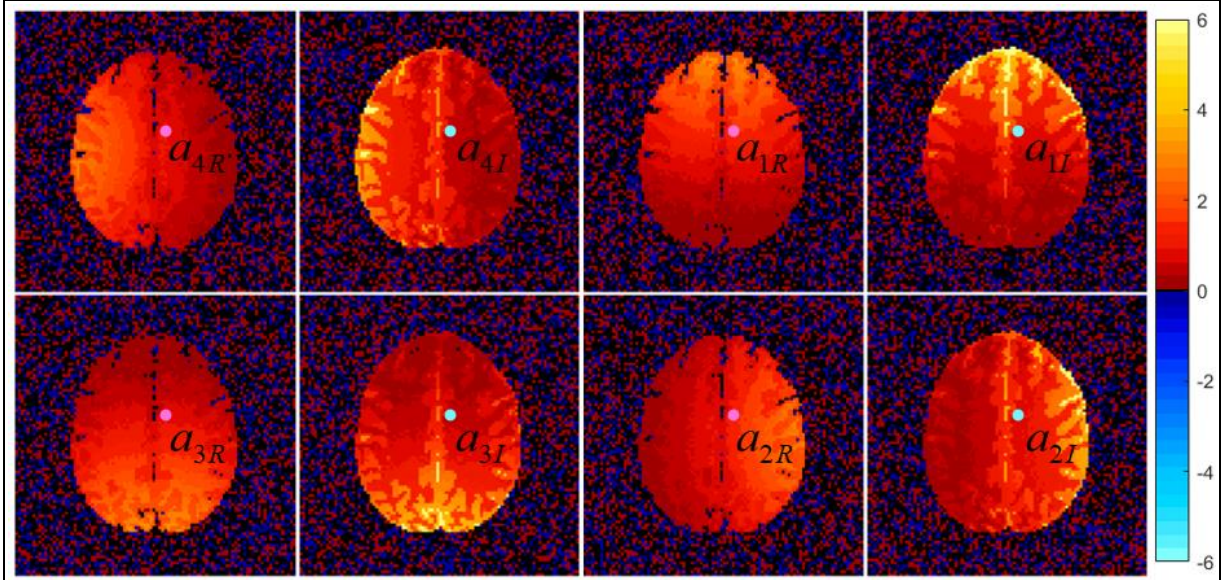


Figure 3.1: Average of m real and imaginary calibration images for the n_C coils.

an fMRI experiment. These n_{cal} calibration images are averaged together to give us the simulated data shown in Figure 3.1. The Euclidean norm in each voxel is computed from these $n_C = 4$ complex-valued coil images in Figure 3.1 for an initial magnitude v_{0M} of the prior mean as in Eq. 3.14.

$$v_{0M} = \left[a_{R1}^2 + a_{I1}^2 + a_{R2}^2 + a_{I2}^2 + a_{R3}^2 + a_{I3}^2 + a_{R4}^2 + a_{I4}^2 \right]^{1/2}. \quad [3.14]$$

The n_C complex-valued averaged calibration images in Figure 3.1 are pointwise divided by the magnitude of the prior mean v_{0M} in order to arrive at the prior mean for the real and imaginary coil sensitivities in Figure 3.2 (top section). The hyperparameters n_S (in Equations 3.3, 3.6, 3.8, 3.9, 3.11, and 3.12) and n_v (in Equations 3.4, 3.6, 3.7, 3.9, 3.10, and 3.12) were set to be the number of calibration images $n_{cal} = 10$. The average residual variance over the voxels of the calibration images were calculated to be $\sigma_0^2 = 0.011$. The hyperparameters α and β in equations 3.4, 3.8, and 3.11 were assessed to be $\alpha = n_{cal} - 1$ and $\beta = (n_{cal} - 1)\sigma_0^2$.

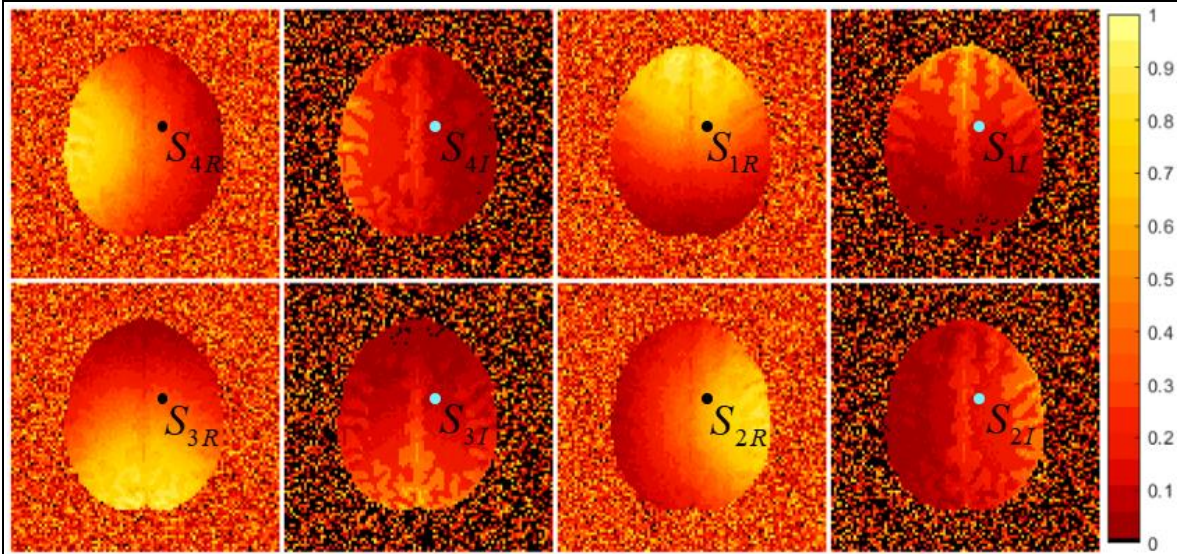


Figure 3.2: Prior mean for coil sensitivities.

4. Simulated Data

4.1 Simulated Data for Single Slice at One Timepoint

A single image at one timepoint was generated for $n_C = 8$ coils by adding $N(0, 0.0025)$ noise, corresponding to a magnitude signal range of 1-6 to the noiseless coil images in Figure 2.2. The

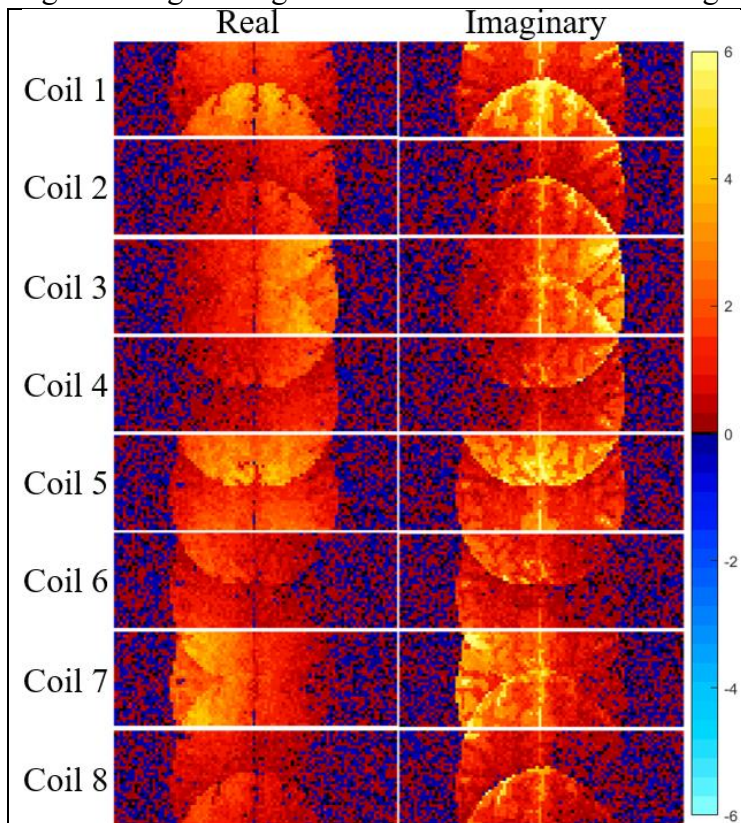


Figure 4.1: Simulated observed noisy coil images for one time point in an fMRI experiment.

derived noisy coil images shown in Figure 4.1 were first aliased followed by adding noise and were used to demonstrate the use of BSENSE.

4.2 Reconstructed Image for Simulated Single Slice at One Timepoint

Using the observed aliased coil images in Figure 4.1, and the assessed hyperparameters, the MAP BSENSE unaliased image was estimated using the ICM algorithm and displayed in Figure 4.2 (left middle). The MCMC Gibbs sampling technique was utilized to estimate the mean of the marginal posterior distribution (middle right in Figure 4.2) using $L = 10,000$ total iterations with a $burn = 2500$. The prior means from the calibration images for the unaliased voxels v and the sensitivity coils S were used as initial values for H and v . These initial values were used to generate a σ^2 value from the posterior conditional from Eq. 3.11, initializing the Gibbs sampler. We can see that the joint MAP estimate using the ICM algorithm and the marginal posterior mean of the MCMC Gibbs sampler for BSENSE image reconstruction produce images that closely resemble

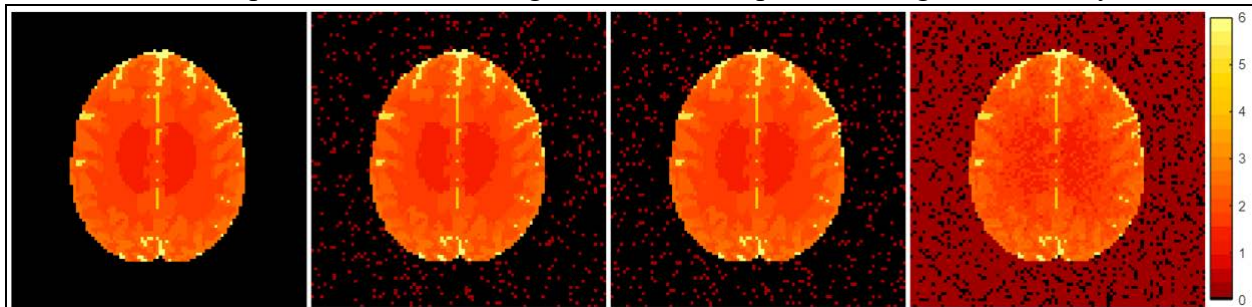


Figure 4.2: True non-task unaliased image (left), BSENSE MAP unaliased non-task magnitude image (left middle) using ICM, Posterior Mean BSENSE unaliased non-task magnitude image (right middle) using Gibbs sampling, and SENSE non-task magnitude image (right).

the true non-aliased image in Figure 4.2 (left). The SENSE image reconstruction produced an image with a higher noise level with less clear distinction between the different brain tissue when compared to BSENSE and the true unaliased image. This is also evident by examining the noise level outside of the brain which is markedly higher in the SENSE reconstructed image. The process illustrated here for reconstructing a single aliased coil image can be replicated to reconstruct the rest of the series.

4.3 Task Activation

The objective of fMRI is to have the patient perform a task, like tapping their fingers, and to capture in which part of the brain increased neuronal activation occurs. The non-task reconstructed images essentially create a baseline value for each voxel giving us an intercept only simple linear regression $y = \beta_0$, where y is the estimated voxel value. By adding in task activation to a certain number of images in the series of images, we then have a simple linear regression $y = \beta_0 + x\beta_1$ for our estimated voxel values. In this regression, β_0 is the baseline voxel value from the non-task reconstructed images determining the SNR, which is β_0/σ , and β_1 is the estimated increase from β_0 which would be the contrast-to-noise ratio (CNR), calculated by β_1/σ . The vector x is a vector of zeros and ones where the zeros correspond to the images in the series without task activation and ones corresponding to the images with task activation. We can write this regression as $y = X\beta$

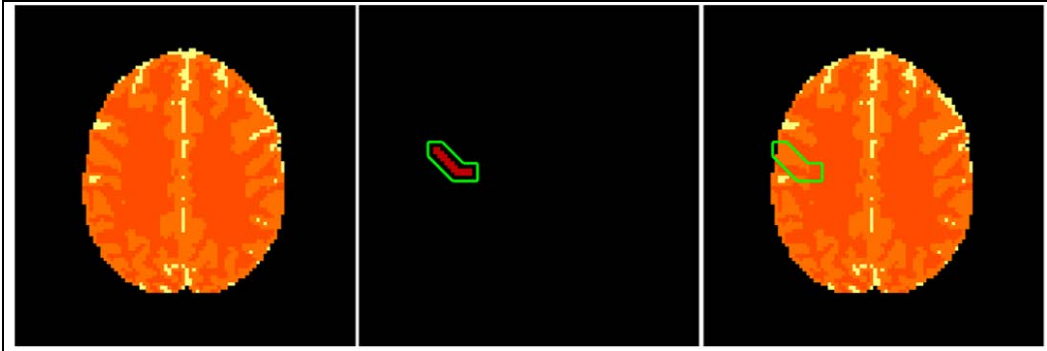


Figure 4.3: Adding magnitude-only task activation (middle) to the true noiseless image (left) to create the true task activation image (right)

where X is our $n_{IM} \times 2$ design matrix with ones in the first column and zeros and ones in the second column and β is a 2×1 vector containing $[\beta_0, \beta_1]'$.

Since the CNR is typically much lower than the SNR, the task is not usually visible on the final reconstructed image. Instead, a hypothesis test is carried out with $\beta_1 \leq 0$ as the null hypothesis and $\beta_1 > 0$ as the alternative. The reason for the one-sided hypothesis test is because we only anticipate an increase signal from the task activation. A simple one-tailed t -test is implemented to determine if any of the voxels experienced a statistically significant increase in signal (magnitude) from the performed task. This statistic summarizes the observed BOLD response to the task at each voxel. Figure 4.3 shows a $\beta_1 = 0.045$ magnitude-only signal increase being added to the true noiseless image with $\sigma^2 \sim N(0, 0.0025)$ noise yielding a CNR of 0.9. Ranges of tissue signals are 1-1.75 for white matter, 1.75-3 for gray matter, and 4-6 for the cerebral spinal fluid in our simulation to mimic our experimental data.

4.4 Simulated Results

The true noiseless task image along with the true noiseless non-task image was used to create a series of 510 simulated full FOV coil images. To simulate our real-world fMRI experimental process, the series was generated by starting with 20 non-task images. In experimental fMRI, the first few images of the times series have increased signal as the magnetization reaches a steady

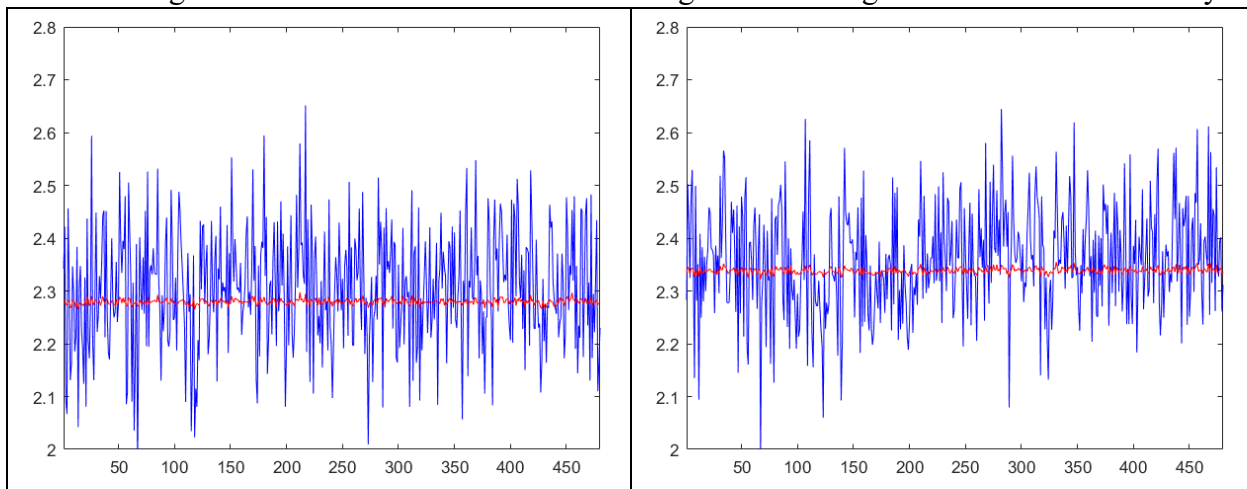


Figure 4.4: Time series of a non-task voxel (left) and time series of a task voxel (right). The blue time series is the SENSE reconstructed voxel and the red time series is the BSENSE MAP estimate.

state. The first image in the simulated series is scaled to increase the signal and used as the superimposed brain images for task detection in Figure 4.5. The scaling was determined by dividing the first few images in the experimental data by the 21st time point, where the magnetization of the machine is stabilized, and calculating the average signal increase for each tissue type. The average signal increase for the white matter was 40%, 55% for the gray matter and 75% for the cerebral spinal fluid (CSF). So, for the first simulated image, the magnitude of the white matter voxels was multiplied by 1.4, the gray matter voxels were multiplied by 1.55, and the CSF voxels were multiplied by 1.75. The initial 20 non-task images are then followed by alternating between 15 non-task images and 15 task images for 16 epochs. The series was culminated with 10 non-task images producing our simulated fMRI series of 510 images. To mimic the fMRI experiment, the first 20 time points were discarded leaving 490 time points in the series. Then the next 10 time points were utilized as our full FOV calibration images to assess the hyperparameters. The remaining 480 points in the time series was first aliased by Fourier transforming the coil images into the spatial frequency domain, skipping lines in k -space, then taking the IFT resulting in aliased coil images. These are reconstructed into full, unaliased images using both SENSE and BSENSE MAP estimation separately. In Figure 4.4 displays the time series of a non-task voxel (left) and the time series of a task voxel (right) with blue line being SENSE reconstructed voxel and the red line being the BSENSE MAP estimate of the reconstructed voxel values. These plots show that the BSENSE method considerably decreases the variance of the voxel values over time, reducing the temporal noise of the series.

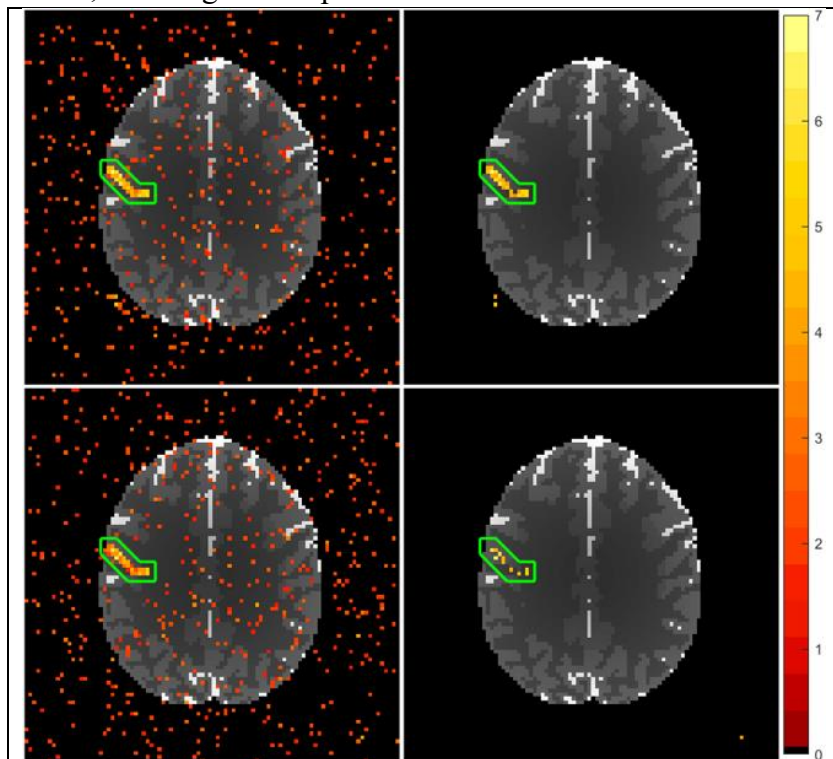


Figure 4.5: Statistically significant voxels using PCER for BSENSE reconstructed images (top left), significant voxels using FDR for BSENSE (top right), significant voxels using PCER for SENSE (bottom left), and significant voxels using FDR for SENSE (bottom right).

The hypothesis test described above was utilized with a 0.05 significance level to determine voxels with a statistically significant signal increase. In Figure 4.5, the left column shows the statistically significant voxels using the per-comparison error rate (PCER) and the right column shows the significant voxels using the 5% false discovery rate (FDR) threshold with BSENSE MAP on top and SENSE on bottom for both columns. The FDR was completed by employing the Benjamini-Hochberg procedure (Benjamini and Hochberg, 1995; Logan and Rowe, 2004) to the p -values from the t -test from each voxel. In the region of interest (ROI), there are 28 voxels with artificially added task activation which both BSENSE and SENSE capture as statistically significant using the PCER. Examining the mean and standard deviation of the t -statistics for both methods we get a mean of 4.7279 and standard deviation of 0.985 for BSENSE and 3.9209 mean and 1.1755 standard deviation for SENSE. However, after applying the FDR, BSENSE identified 25 of the voxels in the ROI as statistically significant while SENSE only identified 10 of the 28 voxels. Along with detecting more voxels as task activation after FDR correction, BSENSE had a notably higher average t -statistic in the ROI and a lower standard deviation. These results indicate BSENSE having a better performance at task detection compared to SENSE.

5. Experimental Data

5.1 Human Subject Data

A 3.0 T General Electric Signa LX magnetic resonance imager was used to conduct an fMRI experiment on a single subject to further compare BSENSE and SENSE. A unilateral right-hand finger-tapping task was performed in a block design with an initial 20 s rest followed by 16 epochs with 15 s off and 15 s on. The experimental was finished off with 10 s of rest giving us a series of 510 TRs (repetitions) with each repetition being 1 second, a flip angle of 90° and an acquisition bandwidth of 125 kHz. The data set comprised of nine 2.5 mm thick axial slices with $n_C = 8$ receiver coils that have a 96×96 dimension for a 24 cm full field of view (FOV), with a posterior to anterior phasing encoding direction. For each volume image in the series, a time dependent echo time, TE_t , consisted of three parts. The first part was fixed to have a value of 42.7 ms at the first 10 time points. In the second part, the next 5 TE values were an equally spaced interval of values 42.7, 45.2, 47.7, 50.2, and 52.7 and was repeated for another 5 time points. For the final part, the last 490 time points were fixed back at 42.7 ms. To account for T_1 effects and varying echo times, the first 20 TRs were discarded leaving 490 time points for the fMRI experiment. The center row of k -space for each TR in each receiver coil was acquired with three navigator echoes which is used to correct any potential Nyquist “ghosting.” The additional rows of k -space were implemented to estimate and adjust the error in the center frequency and group delay offsets between the odd and even lines of k -space (Nencka et al., 2008).

The first 10 time points of the remaining 490 TRs were utilized as pre-scan “calibration” images to assess the hyperparameters for the prior distributions. The remaining 480 TRs were treated as the fMRI experiment. Rows of k -space were censored in each coil for each slice in accordance with an $n_A = 3$ acceleration factor. This means that every two rows of the fully sampled spatial frequencies were removed resulting in a subsampled k -space of dimension 32×96 in each coil for each slice. This causes the images after IFT to be aliased, the same as the aliased images in Figure 4.1, which mimics an experimentally subsampled fMRI dataset. Typically, the B -field gradients in an fMRI experiment will experience a drift in the phase over time which we correct

to give us a stable phase through time. First, the angular phase mean of the time-series is calculated and subtracted for each voxel time-series. A local second order polynomial was fit to the resultant difference of the voxel time-series which. Then the polynomial fitted difference phase is added to a mean phase producing a steady phase over time for each coil.

5.2 Experimental Results

Similar to the process for the simulated data expressed in Section 4.4, the entire times series of aliased coil measurements were simultaneously unaliased and combined using BSENSE MAP estimation and SENSE image reconstruction separately. Figure 5.1 shows the magnitude of our reference image of the 8th slice at the first time point (left), the BSENSE MAP estimate (middle),

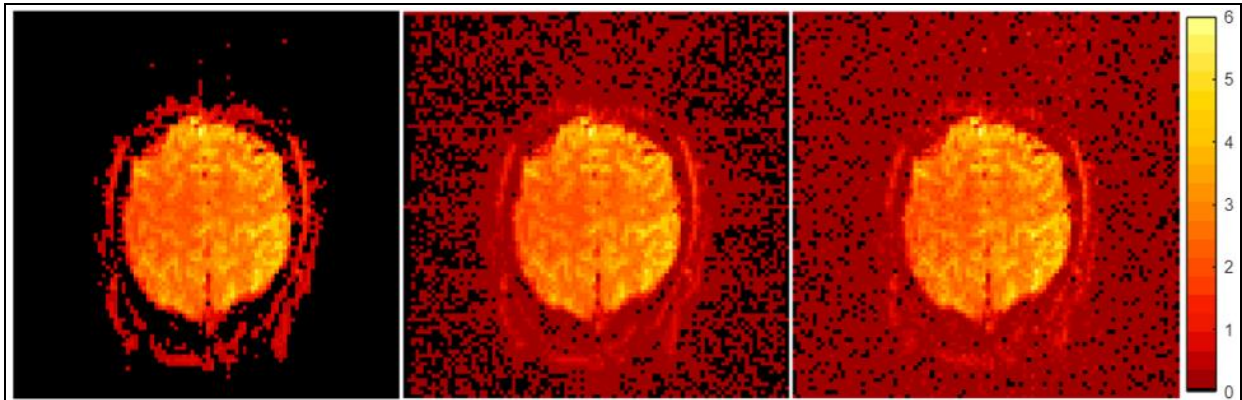


Figure 5.1: Reference non-task unaliased image (left), BSENSE MAP unaliased non-task magnitude image (middle) using ICM, and SENSE non-task magnitude image (right).

and the SENSE reconstructed image (right). Like the simulated results, the BSENSE reconstruction produced a clearer, less noisy image compared to the SENSE reconstruction. It is less noticeable inside of the brain where the SNR is high, but the distinction between the noise level of the two reconstruction processes is more apparent outside the brain. To examine at the noise over time, Figure 5.2 displays the magnitude time series of two voxels one being a non-task voxel (left) and one experiencing task activation (right). The blue colored time series of the SENSE reconstructed voxel, and the red time series of the BSENSE reconstructed voxel. We can see that

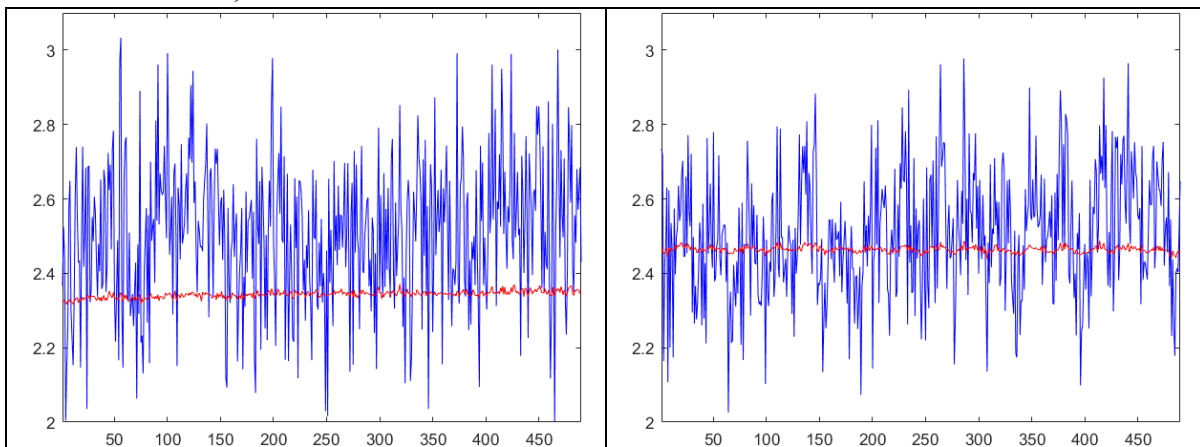


Figure 5.2: Time series of a non-task voxel (left) and time series of a task voxel (right). The blue time series is the SENSE reconstructed voxel and the red time series is the BSENSE MAP estimate.

the variance over time is notably smaller for BSENSE than it is for SENSE, which demonstrates that BSENSE greatly reduces noise variability compared to SENSE resulting in a more accurate image reconstruction over time.

For detection of task activation, the hypothesis test outlined in Section 4.3 was carried out using a 0.05 significance level with 28 voxels in the ROI. The image on the left in Figure 5.3 displays the expected task activation (outlined in green) of the 8th slice after the 5% FDR correction. The image in the middle of Figure 5.3 illustrates the statistically significant voxels using BSENSE and the image on the right shows the statistically significant voxels using SENSE, both after the FDR correction. The mean and standard deviation of our t -statistics in the ROI for SENSE are 4.2365 and 3.5914, respectively. For BSENSE we get a mean t -statistic of 5.4416 and a standard deviation of 3.5634. Both methods exhibit activation in the areas where the task is expected but after the FDR correction, SENSE identified 13 of the 28 voxels with task activation while BSENSE identified 16 of the 28 voxels. Further, BSENSE yielded fewer false positives than SENSE. These results from the experimental data indicate that BSENSE performed better at detecting task than SENSE.

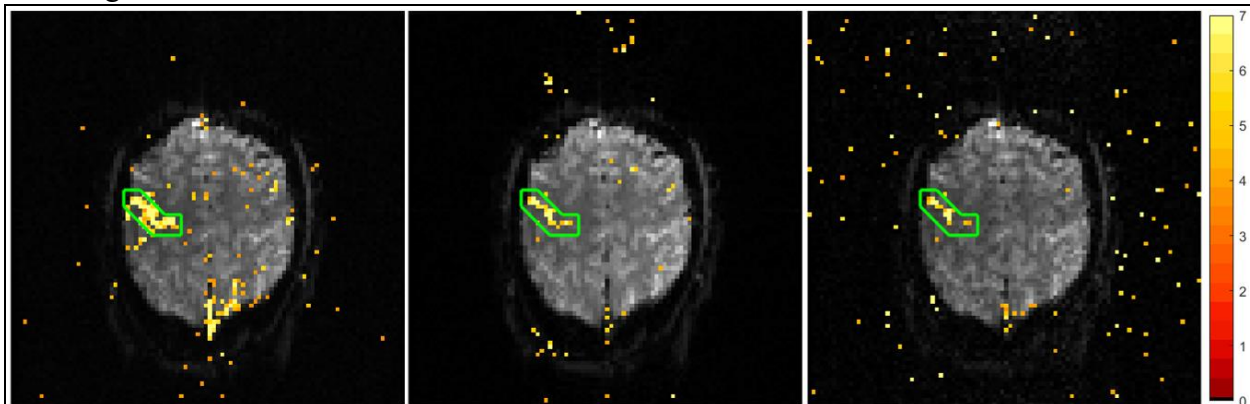


Figure 5.3: Expected task activation of the 8th slice (left), statistically significant voxels using a 5% FDR for BSENSE reconstructed images (middle), and significant voxels using a 5% FDR for SENSE (right).

6. Discussion

6.1 Method and Results Overview

Usage of parallel imaging techniques such as SENSE (Pruessmann et al., 1999) and GRAPPA (Griswold et al., 2002) have accomplished subsampling of k -space and reducing scan times for MR imaging. This could increase the number of images, reconstruct higher resolution images, or a combination of both in the same unit of time as fully sampled k -space. The IFT of the subsampled k -space causes the images to be aliased, so for SENSE image reconstruction, a least squares estimate has been used to unalias the transformed image. This can be difficult to calculate when the design matrix is ill-conditioned, so this paper introduces a Bayesian approach (BSENSE) to estimate the unaliased voxel values. Using more available information from the calibrated images to assess the hyperparameters, this approach successfully reconstructed a single slice simulated brain image using a Bayesian model and a series of simulated slices without any aliasing artifacts. BSENSE also had better performance when detecting the signal increase in the voxels that experienced task activation in the simulated fMRI experiment. Experimental data was also used to

compare the new Bayesian method to the traditional SENSE method and was able to uphold similar results as the simulated experiment.

6.2 Other Advancements

This paper used the full posterior distribution for reconstructing images, meaning available prior information was quantified on all three parameters (S , ν , and σ^2) and utilized for parameter estimation. In addition to the Gibbs sampling technique above to obtain marginal posterior estimates of S , ν , and σ^2 , we have also integrated out σ^2 yielding a reduced posterior where S and ν are the only two unknowns to be estimated. Integrating out σ^2 produces a joint Student- t posterior for S and ν from which we have obtained Gibbs sampling marginal estimates consistent with our three-parameter approach.

For the task detection in this paper, only the MAP estimate using the ICM algorithm was used to reconstruct the simulated series of non-task and task aliased images for capturing activation for both the simulated and experimental data. This is due to the Gibbs sampler being computationally expensive when running a long series of images so it may not be as practical to use compared to evaluating the MAP estimate. This does not mean there is no use for running a Gibbs sampler as the posterior mean does produce similar results to the MAP estimate with the additional benefit of producing entire marginal posterior distributions. For this research, it was used as a technique to confirm proper results from using the ICM to estimate the BSENSE MAP measure. It could be utilized for a shorter series of images or provide us more statistical information about any voxel. This Bayesian approach allows for more options of how to run an fMRI experiment based on the objective of the scan.

6.3 Future Work

Correlation between the unaliased voxels that were previously aliased is a topic that is not covered in this paper (Bruce et al., 2012). An approach to addressing this without changing the model would be to subsample the calibration images at each timepoint and use that data as prior information for those respective timepoints. One circumstance we can consider is increasing the acceleration factor, no greater than the number of coils, and attempt to reconstruct images without having any aliasing artifacts along with capturing any signal increase from task activation. Another can be using a different number and arrangement of coils. Increasing the number of coils does not change the process but it demonstrates the flexibility of the application of this BSENSE. These procedures can also be repeated for vertical aliasing as opposed to the horizontal aliasing used in this research. An extension of the model can be introduced that incorporates both coil covariance and aliased voxel covariance as this current independent model, like SENSE, assumes no correlation between each coil and no correlation between the aliased voxels. The goal of this current research is to introduce BSENSE image reconstruction as an improved parallel imaging technique over SENSE and is expressed through simulated and real-world fMRI experiments.

References

1. Bandettini P, Jesmanowicz A, Wong E, Hyde J. *Processing strategies for time-course data sets in functional MRI of the human brain*. *Mag. Res. Med* 30:161–173, 1993.
2. Benjamini, Y., Hochberg, Y. *Controlling the false discovery rate: a practical and powerful approach to multiple testing*. *J. R. Stat. Soc. B*, 57, 289 – 300, 1995.
3. Bruce IP, Karaman MM, Rowe DB. *A statistical examination of SENSE image reconstruction via an isomorphism representation*. *J. Mag. Res*, 29:1267-1287, 2011.
4. Bruce IP, Karaman MM, Rowe DB. *The SENSE-Isomorphism Theoretical Image Voxel Estimation (SENSE-ITIVE) model for reconstruction and observing statistical properties of reconstruction operators*. *J. Mag. Res*, 30:1143-1166, 2012.
5. Gelfand AE, Smith AFM. *Sampling-Based Approaches to Calculating Marginal Densities*. *Journal of the American Statistical Association*, 85 (410):398-409, 1990.
6. Geman S, Geman, D. *Stochastic Relaxation, Gibbs Distributions, and the Bayesian Restoration of Images*. *IEEE Transactions on Pattern Analysis and Machine Intelligence*. 6(6):721–741, 1984.
7. Griswold MA, Jamob PM, Heidemann RM, Nirkka M, Jellus V, Wang J, Kiefer B, Haase A. *Generalized autocalibrating partially parallel acquisition (GRAPPA)*. *Mag. Res. Med*, 47:1202–1210, 2002.
8. Hoerl AE, Kennard RW. *Ridge Regression: Biased Estimation for Nonorthogonal Problems*. *Technometrics*, 12 (1):69-82, 1970.
9. Hyde JS, Jesmanowicz A, Froncisz W, Kneeland JB, Grist TM, Campagna NF. *Parallel image acquisition from noninteracting local coils*. *J. Mag. Res*, 70:512–517, 1986.
10. Kumar A, Welti D, Ernst RR. *NMR Fourier zeugmatography*. *J. Mag. Res.*, 18(1):69–83, 1975.
11. Lin F-H, Kwong KK, Belliveau JW, Wald LL. *Parallel Imaging Reconstruction using Automatic Regularization*. *Mag. Res. Med*, 51:559–567, 2004.
12. Lindley DV, Smith AFM. *Bayes estimates for the linear model*. *J. R Stat. Soc. B*, 34 (1):1–18, 1972.
13. Liu B, King K, Steckner M, Xie J, Sheng J, Ying L. *Regularized Sensitivity Encoding (SENSE) Reconstruction Using Bregman Iterations*. *Mag. Res. Med*, 61:145-152, 2009.
14. Nencka, A.S., Hahn, A.D., Rowe, D.B. *The use of three navigator echos in cartesian EPI reconstruction reduces Nyquist ghosting*. *Proc. Intl. Soc. Magn. Reson. Med*. 2008; 16.
15. Ogawa S, Lee TM, Nayak AS, Glynn P. *Oxygenation-sensitive contrast in magnetic resonance image of rodent brain at high magnetic fields*. *Mag. Res. Med* 14(1):68–78, 1990.
16. Pruessmann KP, Weiger M, Scheidegger MB, Boesiger P. *SENSE: Sensitivity Encoding for Fast MRI*. *Mag. Res. Med*, 42:952–962, 1999.
17. Rowe DB. *Image Reconstruction in Functional MRI*. In *Handbook of Statistical Methods for Brain Signals and Images*, Editors Ombao H, Lindquist M, Thompson W, Aston J. Chapman & Hall/CRC Press. p. 205-232, 2016.
18. Rowe DB. *Modeling both the magnitude and phase of complex-valued fMRI data*. *Neuroimage*, 25(4):1310–1324, 2005.
19. Rowe DB. *Multivariate Bayesian Statistics: Models for Source Separation and Signal Unmixing*. Chapman & Hall/CRC Press, Boca Raton, FL, 2003.
20. Rowe DB, Bruce IP, Nencka AS, Hyde JS, Kociuba MC. *Separation of parallel encoded*

- complex-valued slices (SPECS) from a single complex-valued aliased coil image*. J. Mag. Res., 34, 359-369, 2016.
21. Rowe DB, Logan BR. *A complex way to compute fMRI activation*. Neuroimage, 23:1078–1092, 2004.
 22. Tibshirani, Robert. *Regression Shrinkage and Selection via the Lasso*. J. R. Stat. Soc. B, 58 (1):267-288, 1996.